Ocean Sci. Discuss., 8, 1777–1802, 2011
www.ocean-sci-discuss.net/8/1777/2011/
doi:10.5194/osd-8-1777-2011

Ocean Science Discussions

A computational method for determining XBT depths

J. Stark[1], J. Gorman[1], M. Hennessey[1], F. Reseghetti[2], J. Willis[3], J. Lyman[4], and J. Abraham[1]

[1]University of St. Thomas, School of Engineering, St. Paul, MN 55105-1079, USA
[2]ENEA, UTMAR-OSS, Forte S. Teresa, 19032 Pozzuolo di Lerici, Italy
[3]Jet Propulsion Laboratory, California Institute of Technology, Pasadena, CA 91109, USA
[4]Pacific Marine Environmental Laboratory/NOAA, Seattle, WA 98115-6349, USA

Received: 13 June 2011 – Accepted: 19 July 2011 – Published: 2 August 2011

Correspondence to: J. Abraham (jpabraham@stthomas.edu)

Published by Copernicus Publications on behalf of the European Geosciences Union.

Abstract

A new technique for determining the depth of expendable bathythermographs (XBTs) is developed. This new method combines a forward-stepping calculation which incorporates all of the forces on the XBT devices during their descent. Of particular note are drag forces which are calculated using a new drag coefficient expression. That expression, obtained entirely from computational fluid dynamic modeling, accounts for local variations in the ocean environment. Consequently, the method allows for accurate determination of depths for any local temperature environment. The results, which are entirely based on numerical simulation, are compared with an experimental descent of an LM-Sippican T-5 XBT. It is found that the calculated depths differ by less than 3 % from depth estimates using the industry standard FRE. Furthermore, the differences decrease with depth. The computational model allows an investigation of the fluid patterns along the outer surface of the probe as well as in the interior channel. The simulations take account of complex flow phenomena such as laminar-turbulent transition and flow separation.

1 Introduction

Accurate determination of the long-term trends in ocean heat content are essential for estimations of the impact of global warming on the planet. The ocean represents a significant reservoir and reacts slowly to changes in the Earth's energy balance. The lag in ocean-thermal response and the very large heat capacity of the ocean waters results in a significant portion of heat being absorbed there and is therefore critical for accurate prediction of future climate change.

Measurements of ocean heat content are made by a variety of devices and techniques have changed over the past century. Today, the water column measurements are most commonly made with expendable bathythermographs (XBT), conductivity/temperature/depth probes (CTD), or Argo floats and gliders. Among these devices, the XBT is the oldest and has the lowest measurement resolution, however

OSD
8, 1777–1802, 2011

the large number of XBTs released annually and the significant number of XBT measurements in the literature ensure that their role in ocean monitoring continues to be important.

Biases in XBT fall rates have led to errors in estimates of overall ocean heating and sea level rise (Gouretski and Koltermann, 2007; Levitus et al., 2005, 2009; Wijffels et al., 2008). XBT biases have been a topic of investigation for decades (Hanawa and Yoritaka, 1987; Heinmiller et al., 1983; Prater, 1991; Seaver and Kuleshov, 1982). Typically, those studies involved the simultaneous release of XBT probes with more accurate CTD devices. Comparisons of temperature profiles allow a determination of the bias, which depend on errors in estimated depths and on a thermal bias due to temperature sensing electronics (CTD depths and temperatures were considered exact).

Currently, multiple classes of XBT probes are manufactured but the most common are referred to as T4/T6/T7/DB class and the T5 class. There are slight geometric differences between the classes of XBT devices and therefore, it is expected that there are slightly different fall characteristics. Additionally, the devices are manufactured by two different companies (LMSippican and TSK) and the manufacturing processes since the 1960s could have introduced variations in the geometry of the probes. Finally, alterations made to the devices in subsequent generations have led to variations in behavior so that year-to-year consistency is not guaranteed (Wijffels et al., 2008; Gouretski and Reseghetti, 2010; Johnson, 2010; Kizu, 2010; Goni and Di Nezio, 2010; Reseghetti, 2010).

With respect to the fall rate equations (FRE) originally supplied by L. M. Sippican, the inventor of the XBT probes, several works have tried to provide improvements over the manufacturer recommendations for the various XBT models. Most of them concern the T4/T6/T7/DB class and are summarized by Hanawa (1995). The FRE proposed by Hanawa (1995) has been considered the industry standard for the T4/T6/T7/DB class. Only a few reports analyzed the T5 class (Boyd and Linzell, 1993; and Kizu, 2005). Nevertheless, it has been argued that these FRE models cannot be universally applied

OSD
8, 1777–1802, 2011

around the globe with consistent accuracy. Specifically, there are experimental indications that the probe fall rate depends on the local water temperature (Hanawa, 1995; Green, 1984; Thadathil et al., 2002; Kizu et al., 2005). Since the current FREs originated in experiments performed in tropical or subtropical waters, their application to polar regions or to water bodies with temperatures differing from tropic regions may not be appropriate. Furthermore, use of the standard FRE outside their range of applicability has a significant impact on ocean heat content (Gouretski and Reseghetti, 2010).

It is believed that the dependency of FRE models on local conditions is a critical limitation to their accuracy, particularly when they are to be applied in different environments. Consequently, a new approach is proposed which calculates the fall rate of XBT devices for any local conditions. This method takes advantage of local temperature measured by the XBT itself to auto-correct for biases in the FRE. This new method requires very accurate determinations of the drag coefficient and its variation with Reynolds number. The calculation of the drag coefficient will be performed with greater fidelity than the earlier estimates of drag (Green, 1984; Hallock and Teague, 1992). While those earlier efforts were seminal and pioneering, the research was limited by the ability to accurately determine the drag coefficient.

Advances in computational modeling now allow the aforementioned limitation to be overcome. Numerical analysis of the fluid dynamics can account for details in physical geometry of the probe and complex mechanics in the fluid. Included here is the accounting of laminar-turbulent transition of the fluid boundary layer against the probe body.

Here, a mathematical model will be presented to determine the depth of an XBT T-5 probe during a recent experimental launch. The method is not fully predictive because it relies upon local temperature measurements made by the probe for the determination of depth. The results will make use of previously calculated drag coefficients that were obtained using numerical simulation. Probe depth will be determined with a forward-stepping time integration.

OSD
8, 1777–1802, 2011

2 Numerical model

The numerical model has two important components. The first is the depth-calculation algorithm, second are the results for the Reynolds-dependent drag coefficient. Both portions of the numerical procedure will now be presented.

2.1 Depth calculations

The depth of the probe is based on a force-balance which is shown in Eq. (1). It can be seen that the net force on the probe is a combination of buoyancy and drag forces. Their difference is equal to the change in probe momentum. Changes in momentum arise from both velocity variations as well as variations in the mass as the transmitting wire unspools.

$$F_{\text{net}} = F_{\text{buoy}} - F_{\text{drag}} = \frac{d\left(m_{\text{p}}V\right)}{d} = m_{\text{p}}\frac{dV}{dt} + V\frac{dm_{\text{p}}}{dt} \tag{1}$$

The term m_{p} represents the instantaneous mass of the probe and dm_{p}/dt is the rate at which that mass decreases from wire loss. The buoyant force is equal to the difference in the probe weight and the weight of displaced water, $m_{\text{w}}g$; so that

$$F_{\text{buoy}} = \left(m_{\text{p}} - m_{\text{w}}\right)g \tag{2}$$

whereas the drag force is found from the classic definition of the drag coefficient to be

$$F_{\text{drag}} = C_{\text{d}}\frac{1}{2}\rho V^2 A \tag{3}$$

Where ρ is the local water density, V is the probe velocity and A is the frontal area of the probe. When Eqs. (1)–(3) are combined and the chain rule of differentiation is applied, there is obtained

$$\left(m_{\text{p}} - m_{\text{w}}\right)g - C_{\text{d}}\frac{1}{2}\rho V^2 A = m_{\text{p}}\frac{dV}{dx}\frac{dx}{dt} + V\frac{dm_{\text{p}}}{dx}\frac{dx}{dt} = m_{\text{p}}V\frac{dV}{dx} + V^2\frac{dm_{\text{p}}}{dx} \tag{4}$$

OSD
8, 1777–1802, 2011

Which can be rearranged to give

$$\frac{dV}{dx} = \frac{\left(m_\mathrm{p} - m_\mathrm{w}\right) g - C_\mathrm{d} \frac{1}{2} \rho V^2 A - V^2 \frac{dm_\mathrm{p}}{dx}}{m_\mathrm{p} V} \tag{5}$$

This model accounts for variations in the XBT velocity with depth but it does not account for unsteadiness in the ocean currents, that is, it assumes a quiescent water body.

While Eq. (5) is a viable representation of the variation in probe velocity, it is not solvable for velocity. Consequently, a finite-difference discretization is applied to Eq. (5) to give, after rearrangement

$$V^\mathrm{new} = V + \frac{\Delta t}{m_\mathrm{p}} \left[\left(m_\mathrm{p} - m_\mathrm{w}\right) g - C_\mathrm{d} \frac{1}{2} \rho V^2 A - V^2 \frac{dm_\mathrm{p}}{dx} \right] \tag{6}$$

where V^new is the velocity at a future time step. All terms on the right-hand side of Eq. (6) are evaluated at a current time so that this numerical model marches forward. Provided that the initial conditions of the launch (initial velocity and mass) are known, this equation can be evaluated. It must be emphasized that the use of Eq. (6) obviates the need for a traditional FRE which relates depth to fall time. Equation (6) will, when accompanied with an expression for the drag coefficient, determine the depth of an XBT for any local environment.

2.2 Determination of the drag coefficient

Notably, the drag coefficient on the right-hand side of Eq. (6) must be known at each time step in order to proceed with the numerical integration. It is impossible to determine drag coefficients analytically on blunt objects which cause flow separation. Either experimental or computational investigations are required. Computational investigations offer a significant advantage over experimentation because of the ability to carefully control operating parameters and to determine drag coefficients for a wide variety of operating conditions. Typically, drag coefficients are found to be singular functions

OSD
8, 1777–1802, 2011

of the Reynolds number. Since the Reynolds number is, itself, a function of the local temperature, velocity, and viscosity of the fluid, it follows that

$$C_d = \text{function}(Re^{old}) = \text{function}(T, V, \mu) \quad (7)$$

With Eq. (7) available, the integration expressed in Eq. (6) can be completed.

2.3 The computational model

The first step in the determination of the drag coefficient is the discretization of the fluid region surrounding the probe. That discretization can be seen in Fig. 1. This figure shows a bisected view of the probe and the mesh which spans the fluid domain. The mesh deployment was based on the knowledge of important processes which occur in the boundary layer. These boundary-layer processes govern the development of shear stress and pressure drag. It is essential for the elements to be fine within the boundary layer and aligned with the flow so that processes such as laminar-to-turbulent transition and boundary layer growth can be determined. It can be seen from Fig. 1 that the computational model extends around the exterior of the probe but also includes the flow that passes through the center channel of the device.

The governing equations include mass conservation, momentum conservation, turbulence, and two transport equations which govern the laminar-to-turbulent transition process. Each equation is solved at every computational element within the solution domain. This computational method, often termed the *finite-volume method*, is well established with a history of accurate fluid simulations.

The first equation in the set, conservation of mass, is expressed in tensor notation as

$$\frac{\partial u_i}{\partial x_i} = 0 \quad (8)$$

OSD
8, 1777–1802, 2011

The term u_i is the local velocity in the i-th direction. The next set contains three individual equations which represent conservation of momentum in the three coordinate directions. Mathematically, it appears as

$$\rho\left(u_i\frac{\partial u_j}{\partial x_j}\right) = -\frac{\partial p}{\partial x_j} + \frac{\partial}{\partial x_j}\left((\mu+\mu_{\text{turb}})\frac{\partial u_j}{\partial x_j}\right) j = 1,2,3 \tag{9}$$

Here, ρ is the local fluid density, p, is the pressure, μ is the molecular viscosity of the fluid, and the term μ_{turb} is the turbulent viscosity which is related to local fluctuations in the fluid velocity associated with turbulent motion.

A critical step in a computational fluid simulation is the determination of the turbulent viscosity. A variety of methods have been used to accomplish this step, following the pioneering work of Spalding and Launder (Spalding and Launder, 1974) and of Wilcox (Wilcox, 1988, 1994). More recent developments have combined the best features of these works into a comprehensive turbulent solution algorithm. That new approach was first proposed by Menter (Menter, 1994) and is often termed the *Shear Stress Transport Model (SST)*. The SST model has shown excellent capabilities of predicting flow separation, wall shear, and pressure variations in boundaries of blunt objects, such as XBT probes.

The SST model makes use of two transport equations for the turbulent kinetic energy κ, and the specific rate of turbulent dissipation, ω. Those transport equations are

$$\frac{\partial(\rho u_i\kappa)}{\partial x_i} = \gamma\cdot P_\kappa - \beta_1\rho\kappa\omega + \frac{\partial}{\partial x_i}\left[\left(\mu+\frac{\mu_{\text{turb}}}{\sigma_\kappa}\right)\frac{\partial\kappa}{\partial x_i}\right] \tag{10}$$

and

$$\frac{\partial(\rho u_i\omega)}{\partial x_i} = A\rho S^2 - \beta_2\rho\omega^2 + \frac{\partial}{\partial x_i}\left[\left(\mu+\frac{\mu_{\text{turb}}}{\sigma_\omega}\right)\frac{\partial\omega}{\partial x_i}\right] + 2(1-F_1)\rho\frac{1}{\sigma_{\omega 2}\omega}\frac{\partial\kappa}{\partial x_i}\frac{\partial\omega}{\partial x_i} \tag{11}$$

A full description of the SST model and the terms in Eqs. (10) and (11) are provided in Menter (1994).

OSD
8, 1777–1802, 2011

The solution of coupled Eqs. (10) and (11) yields the values for the turbulent viscosity which is expressed as

$$\mu_{\text{turb}} = \frac{a\rho\kappa}{\max(a\omega, SF_2)} \tag{12}$$

The final stage in the numerical procedure is to predict the status of the flow (laminar, intermittent, or turbulent). Most flow situations involve fluid motion that is a combination of these three states. For instance, flow near the leading edge of the XBT nose is likely to be laminar whereas flow near the aft is likely to be turbulent. There is a transitional region between the laminar and turbulent zones where the flow is partly laminar and partly turbulent. This laminar-to-turbulent transition is known to affect drag significantly (Gorman et al., 2010).

The transitional model used here was developed by Menter (Menter et al., 2002, 2004a, b) and later used by the present authors in a series of studies that conclusively demonstrated its suitability for flows of this nature (Abraham et al., 2008, 2009, 2010; Abraham and Thomas, 2009; Thomas and Abraham, 2010; Minkowycz et al., 2009; Sparrow et al., 2009; Lovik et al., 2009).

The transition model consists of transport equations for the turbulent intermittency γ, and the turbulent adjunct function Π. Those models are expressed as

$$\frac{\partial(\rho\gamma)}{\partial t} + \frac{\partial(\rho u_i \gamma)}{\partial x_i} = P_{\gamma,1} - E_{\gamma,1} + P_{\gamma,2} - E_{\gamma,2} + \frac{\partial}{\partial x_i}\left[\left(\mu + \frac{\mu_{\text{turb}}}{\sigma_\gamma}\right)\frac{\partial\gamma}{\partial x_i}\right] \tag{13}$$

and

$$\frac{\partial(\rho\Pi)}{\partial t} + \frac{\partial(\rho u_i \Pi)}{\partial x_i} = P_{\Pi,t} + \frac{\partial}{\partial x_i}\left[\sigma_{\Pi,t}(\mu + \mu_{\text{turb}})\frac{\partial\Pi}{\partial x_i}\right] \tag{14}$$

Further details about the models can be found in the referenced literature.

The boundary conditions were applied far enough from the probe to ensure that their placement did not affect the results. At the inlet, positioned 0.45 m upstream of the probe, a uniform relative velocity was given. At the exit, which was located

OSD
8, 1777–1802, 2011

0.64 m downstream from the probe, an average gauge pressure was applied with weak conditions on all transported variables. At the probe surface, standard no slip conditions were employed. At lateral boundary conditions, which were positioned at least 7.5 cm from the probe, free-slip conditions were used. The simulations used a total of 2 100 000 elements and the results were found to be independent of mesh size. All calculations were performed using ANSYS CFX V12.1 software. In these simulations, no account was made for rotation of the probe during its descent. Further studies will be performed in the near future to account for this effect.

Numerous simulations were completed for a range of velocities and viscosity values. Table 1 lists the parameters for the individual simulations. In these calculations, the water density was treated as a constant and equal to 1025 $kg\,m^{-3}$. The frontal area of the T5 probe was found to be 0.00206 m^2 and the probe length is 0.342 m. The characteristic length in the Reynolds number is taken to be the probe length.

3 Results and discussion

Results from the numerical simulations will be presented first in a qualitative manner with a focus on the flow patterns which occur along the body of the T5. Next, quantitative results of the drag coefficients will be provided. Finally, the drag coefficients will be used to estimate the depth of a T5 when data on temperature and fall-time are available. Figure 2 shows a set of velocity contour diagrams near the (a) leading edge of the probe and in the (b) rear of the probe. The results in this figure and the following figure are representative of the set of results obtained using the information in Table 1.

Notable and expected features are easily observed. First, there is a local slow-fluid zone at the forward cone of the probe, near the center channel inlet. Second, it can be seen that fluid passes through the center channel and complicated recirculation regions are seen within the cavity. Finally, a recirculation region is seen behind the probe with relatively low velocities.

OSD
8, 1777–1802, 2011

More details of the actual flow patterns are provided in Fig. 3 which shows two images of streamlines near the (a) nose of the probe and (b) in the interior cavity of the probe. The figure clearly shows that fluid enters the probe channel with a longitudinally directed motion however the flow separates from the channel walls and experiences recirculation at the cavity enlargement.

The critical result which is required for the estimation of probe depth is the drag coefficient. In the present simulations, drag was found from Eq. (3) where the drag force was found from the simulations. The listing of results is shown in Table 2, along with a comparison to results which would be obtained with the estimation that is recommended in Green (1984). Graphical comparison of the present results with those of Green (1984) are shown in Fig. 4.

There are a number of features which are evident from the figure. First, the numerical simulations show a drag coefficient that is singularly dependent on the Reynolds number. This finding is reassuring because it is expected from basic fluid-mechanic theory. Second, it can be seen that the present results show values of the drag coefficient which consistently exceed those of Green (1984). In the figure, a fit of the presently calculated drag coefficient to Reynolds number is shown with the resulting expression

$$C_{\mathrm{d}} = 2.74 \times 10^{-15} \cdot Re^2 - 2.21 \times 10^{-8} \cdot Re + 0.1668 \quad (15)$$

The results of the present work also display a greater dependency of the drag coefficient on Reynolds number. It is relevant to identify a rational basis for the disagreement of the drag coefficients of the present work with those of Green (1984). Green's results were taken from literature that presented drag values for streamlined bodies with controlled turbulence (Hoerner, 1965). That work provided only generalized values for various streamlined shapes. Generalized models are incapable of providing probe-specific drag results. Although the work of Hoerner (1965) and the incorporation of drag into probe depth calculations was very advanced at the time, it was, admittedly, limited by the information that was available.

OSD
8, 1777–1802, 2011

The new drag coefficient and the numerical algorithm of Eq. (7) were applied to a recent T5 test. The tests were carried out on 2 May 2011 in the Mediterranean Sea and were compared to numerical predictions. The parameters using in the simulations are listed in Table 3.

A comparison between the predicted depth using the current manufacturer supplied FRE and the present results is displayed in Fig. 5. The level of agreement is striking, considering that the present predicts are based solely on numerical simulations. It can be seen that the present results slightly overestimate the depth of the probe compared to the manufacturer supplied FRE. This behavior can be explained by a number of reasons. First, the simulations were performed on a non-rotating probe. Second, the simulations were performed on a probe that may have had slight differences in geometry or weight from that which was used in the experiments. Furthermore, the comparisons are based off of a single experiment. Deviations from one experiment to the other may also give rise to some of the differences noted here. It is expected that when rotational motion is considered, the results will be brought into even closer agreement. Also shown in Fig. 5 are the depth results using the Boyd and Linzell (1993) FRE. It can be seen the all three results are virtually indistinguishable from each other.

A more useful comparison is shown in Fig. 6. That figure shows the percentage deviation between the present results and those of the manufacturer supplied FRE. It can be seen that the results differ by less than 3 % and the deviation decreases with depth.

A final way to compare the present results with those using the manufacturer supplied FRE is to show the temperature/depth relationship. This information is provided in Fig. 7. That figure shows results of both the present method with those from the Sippican FRE. The Sippican FRE results were extracted from a 2010 drop performed in the Mediterranean Sea using a T-5 XBT. It can be seen, at least on the scale shown in the figure, that the results are virtually indistinguishable from each other. This close agreement lends strong support to the fully computational method of calculating XBT T-5 depths.

OSD
8, 1777–1802, 2011

4 Concluding remarks

This work presents a novel treatment of calculating the depth of an XBT device during an oceanographic measurement. The method takes advantage of advanced computational fluid dynamic software to calculate the drag coefficient with Reynolds number. Twelve separate calculations were performed for a non-rotating T5 device. It was found that the drag coefficient did not depend separately on the various operating parameters but rather depended solely on the value of the Reynolds number. This result concurs with expectations. The newly found drag coefficient is expected to be significantly more accurate than prior estimates which were based on experimental or analytical approximations.

The drag coefficient results were input into a new method for determining the probe depth. This new method is based solely on probe dynamics and force balances. A significant advantage of the present method is that it can be applied for any local environmental conditions such as water temperature. The method takes advantage of the temperature measurements made by the probe during its descent. The temperatures are utilized to determine instantaneous Reynolds numbers and subsequent drag coefficients. This method avoids the reliance upon traditional fall rate equations.

The method was applied to a T5 experiment where it was found that the model agreed with the manufacturer supplied FRE to within 3 %. The agreement improved with depth. Finally, the computational method allows an evaluation of the flow patterns in the near vicinity of the probe and of the flow within the probe's central channel.

The most important result which stems from this work is that it will be possible to re-evaluate the historical archive of T-5 XBT data in order to improve the past records of ocean heat content. The reappraisal of past XBT data will now be able to take account of local temperature conditions without reliance upon a standard FRE. The reappraisal will simply require a forward integration of Eq. (6) with the drag coefficient from Eq. (15) used as input. Presently, a similar effort is being carried out on the T4/T6/T7/DB class XBT devices.

OSD
8, 1777–1802, 2011

References

Abraham, J. and Thomas, A.: Induced Co-Flow and Laminar-to-Turbulent Transition with Synthetic Jets, Comput. Fluids, 38, 1011–1017, 2009.

Abraham, J., Tong, J., and Sparrow, E.: Breakdown of Laminar Pipe Flow into Transitional Intermittency and Subsequent Attainment of Fully Developed Intermittent or Turbulent Flow, Num. Heat. Tran. B, 54, 103–115, 2008.

Abraham, J., Sparrow, E., and Tong, J.: Heat Transfer in All Pipe Flow Regimes – Laminar, Transitional/Intermittent, and Turbulent, Int. J. Heat Mass Tran., 52, 557–563, 2009.

Abraham, J. P., Sparrow, E. M., Tong, J. C. K., and Bettenhausen, D. W.: Internal Flows which Transist from Turbulent Through Intermittent to Laminar, Int. J. Therm. Sci., 49, 256–263, 2010.

Boyd, J. and Linzell, R.: The Temperature and Depth Accuracy of Sippican T-5 XBTs, J. Atmos. Ocean Tech., 10, 128–139, 1993.

Goni, G.: NOAA/AOML hydrographic Efforts to Assess the FRE and Evaluate Different Acquisition Systems, XBT Bias and Fall Rate Workshop, Hamburg, Germany, 25–27 August 2010.

Gorman, J. M., Sherrill, N. K., and Abraham, J. P.: Analysis of Drag-Reducing Techniques for Olympic Skeleton Helmets, ANSYS Users Conference, Minneapolis, MN, 11 June 2010.

Gouretski, V. and Koltermann, K.: How Much is the Ocean Really Warming: Geophys. Res. Lett., 34, L01610, doi:10.1029/2006GL027834, 2007

Gouretski, V. and Reseghetti, F.: On Depth and Temperature Biases in Bathythermograph data: Development of a New Correction Scheme Based on Analysis of a Global Ocean Database, Deep-Sea Res. Pt. 1, 57, 812–833, 2010.

Green, A.: Bulk Dynamics of the Expendable Bathythermograph, Deep-Sea Res., 31, 415–426, 1984.

Hallock, Z. and Teague, W.: The Fall Rate of the T-7 XBT, J. Atmos. Ocean Tech., 9, 470–483, 1992.

Hanawa, K. and Yoritaka, H.: Detection of Systematic Errors in XBT Data and Their Correction, J. Ocean. Soc. Japan, 43, 68–76, 1987.

Hanawa, K., Rual, P., Bailey, R., Sy, A., and Szabados, M.: A New Depth-Time Equation for Sippican or TSK T-7; T-6; and T-4 Expendable Bathythermographs (XBT), Deep-Sea Res., 42, 1423–1451, 1995.

OSD
8, 1777–1802, 2011

Heinmiller, R., Eddesmeyer, C., Taft, B., Olson, D., and Nikitin, O.: Systematic Errors in Expendable Bathythermograph (XBT) Profiles, Deep-Sea Res., 30, 1185–1197, 1983.
Hoerner, S.: Fluid-Dynamic Drag, Hoerner Dynamics, Bricktown, NJ, 1965.
Johnson, G.: Echo Sounder Evaluation of XBT Drop Rate Off the Coast of Florida, XBT Bias and Fall Rate Workshop, Hamburg, Germany, 25–27 August 2010.
Kizu, S.: Evaluation of the Fall Rate of Recent T-7 Probes Manufactured by Sippican and TSK, XBT Bias and Fall Rate Workshop, Hamburg, Germany, 25–27 August 2010.
Kizu, S., Yoritaka, H., and Hanawa, K.: A New Fall-Rate Equation for T-5 Expendable Bathythermograph (XBT) by TSK, J. Oceanography, 61, 115–121, 2005.
Launder, B. and Spalding, D.: Mathematical Modeling of Turbulence, Comput. Method. Appl. M., 3, 269–289, 1974.
Lovik, R. D., Abraham, J. P., Minkowycz, W. J., and Sparrow, E. M.: Laminarization and Turbulentization in a Pulsatile Pipe Flow, Num. Heat. Tran. A, 56, 861–879, 2009.
Levitus, S., Anotonov, J., and Boyer, T.: Warming of the World Oceans, Geophys. Res. Lett., 32, L12602, doi:10.1029/2004GL021592, 2005.
Levitus, S., Antonov, J., Boyer, T., Locarnini, R., Garcia, H., and Mishonov, A.: Global Ocean Heat Content 1955–2008 in Light of Recently Revealed Instrumentation Problems, Geophys. Res. Lett., 36, L07608, doi:10.1029/2008GL037155, 2009.
Menter, F.: Two Equation Eddy-Viscosity Models for Engineering Applications, AIAA J., 32, 1598–1605, 1994.
Menter, F., Esch, T., and Kubacki, S.: Transition Modelling Based on Local Variables, 5th Int. Symposium on Engineering Turbulence Modeling and Measurements, Mallorca, Spain, 2002.
Menter, F., Langtry, R., Likki, S., Suzen, Y., Huang, P., and Volker, S.: A Correlation-Based Transition Model Using Local Variables, Part I – Model Formulation, Proceedings of ASME Turbo Expo Power for Land, Sea, and Air, Vienna, Austria, 14–17 June 2004a.
Menter, F., Langtry, R., Likki, S., Suzen, Y., Huang, P., and Volker, S.: A Correlation-Based Transition Model Using Local Variables, Part II – Test Cases and Industrial Applications, Proceedings of ASME Turbo Expo Power for Land, Sea, and Air, Vienna, Austria, 14–17 June 2004b.
Minkowycz, W. J., Abraham, J. P., and Sparrow, E. M.: Numerical Simulation of Laminar Breakdown and Subsequent Intermittent and Turbulent Flow in Parallel Plate Channels: Effects of Inlet Velocity Profile and Turbulence Intensity, Int. J. Heat. Mass. Tran., 52, 4040–4046,

OSD
8, 1777–1802, 2011

2009.
Prater, M.: A Method for Depth and Temperature Correction of Expendable Probes, J. Atmos. Ocean Tech., 8, 888–894, 1991.
Reseghetti, F.: Performance of XBT Systems in Mediterranean Sea (2003–2010), XBT Bias and Fall Rate Workshop, Hamburg, Germany, 25–27 August 2010.
Seaver, G. and Kuleshow, S.: Experimental and Analytical Error of the Expendable Bathythermograph, J. Phys. Oceanogr., 12, 592–600, 1982.
Sparrow, E. M., Abraham, J. P., and Minkowycz, W. J.: Flow Separation in a Diverging Conical Duct: Effect of Reynolds Number and Divergence Angle, Int. J. Heat. Mass. Tran., 52, 3079–3083, 2009.
Thadathil, P., Saran, A., Gopalakrishna, V., Vethamony, P., and Araligidad, N.: XBT Fall Rate in Waters of Extreme Temperature: A Case Study in the Antarctic Ocean, J. Atmos. Ocean Tech., 19, 391–395, 2002.
Thomas, A. and Abraham, J.: Sawtooth Vortex Generators for Underwater Propulsion, Open Mech. Eng., 4, 1–7, 2010.
Wijfeels, S., Willis, J., Domingues, C., Barker, P., White, N., Gronell, A., Ridgeway, K., and Church, J.: Changing Expendable Bathythermograph Fall Rates and Their Impact on Estimates of Thermosteric Sea Rise, J. Climate, 21, 5657–5672, 2008.
Wilcox, D.: Reassessment of the Scale-Determining equations for Advanced Turbulence Models, AIAA J., 26, 1299–1310, 1988.
Wilcox, D.: Comparison of Two-Equation Turbulence Models for Boundary Layers with Pressure Gradients, AIAA J., 31, 1414–1421, 1994.

OSD
8, 1777–1802, 2011

Table 1. Listing of parameters used in simulations.

Case	Velocity ($m\,s^{-1}$)	Kinematic Viscosity ($cm^2\,s^{-1}$)	Reynolds Number
1	6	0.0095	2 141 000
2	6.5	0.0095	2 319 000
3	7	0.0095	2 497 000
4	6	0.0103	1 974 000
5	6.5	0.0103	2 139 000
6	7	0.0103	2 303 000
7	6	0.0136	1 495 000
8	6.5	0.0136	1 620 000
9	7	0.0136	1 744 000
10	6	0.0146	1 393 000
11	6.5	0.0146	1 509 000
12	7	0.0146	1 625 000

OSD
8, 1777–1802, 2011

Table 2. Comparison of calculated drag coefficients with those from Green (1984).

Case	Reynolds Number	Calculated Drag Coefficient	Estimated Drag Coefficient (Green, 1984)
1	2 141 000	0.132	0.116
2	2 319 000	0.131	0.115
3	2 497 000	0.129	0.114
4	1 974 000	0.134	0.117
5	2 139 000	0.132	0.116
6	2 303 000	0.130	0.115
7	1 495 000	0.140	0.119
8	1 620 000	0.138	0.118
9	1 744 000	0.137	0.118
10	1 393 000	0.142	0.120
11	1 509 000	0.140	0.119
12	1 625 000	0.138	0.118

OSD
8, 1777–1802, 2011

Table 3. Parameter values used for fall calculations.

Parameter	Value
Initial probe mass	0.98 (kg)
Mass of wire per unit length	0.000118 ($kg\,m^{-1}$)
Probe length	0.342 (m)
Probe frontal area	0.00203 (m^3)
Launch height	2.5 (m)
Initial probe velocity	7 ($m\,s^{-1}$)
Initial probe displaced volume	0.000274 (m^3)
Wire diameter	0.00762 (cm)
Density of surface water	1028 ($kg\,m^{-3}$)

OSD
8, 1777–1802, 2011

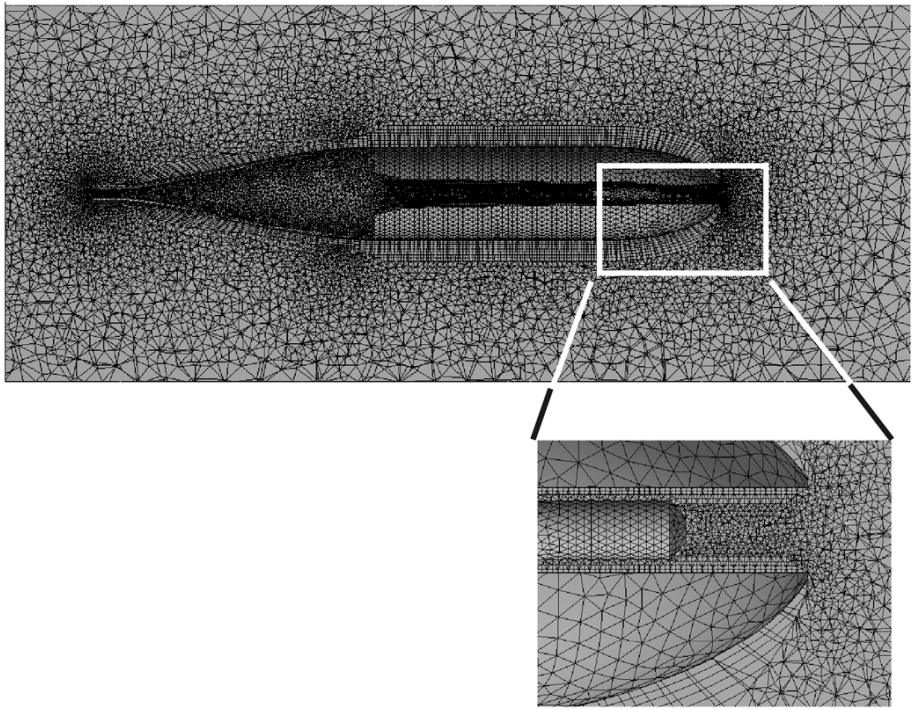

Fig. 1. Image of the computational mesh with a close up view of elements near the probe nose.

OSD
8, 1777–1802, 2011

A computational method for determining XBT depths

J. Stark et al.

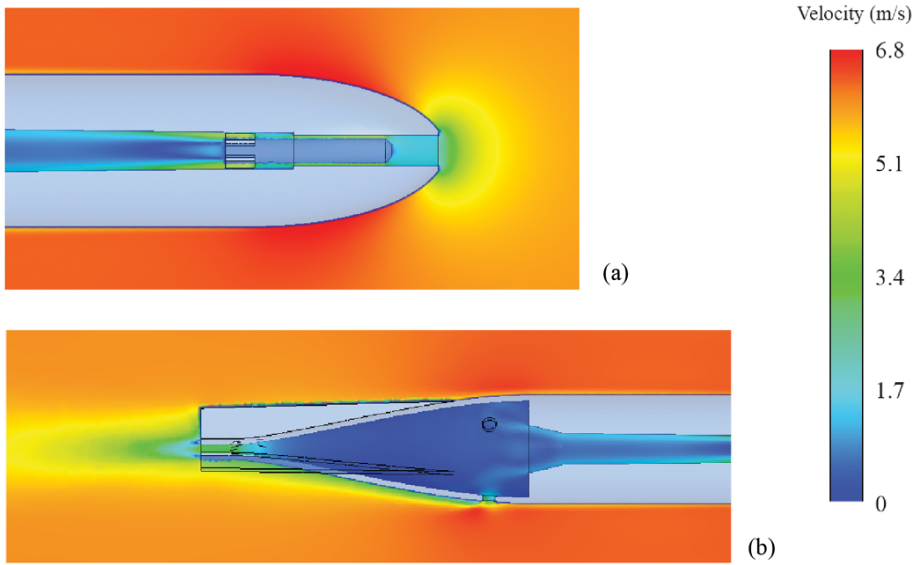

Fig. 2. Velocity contours at the **(a)** leading edge of the probe and **(b)** in the aft region.

OSD
8, 1777–1802, 2011

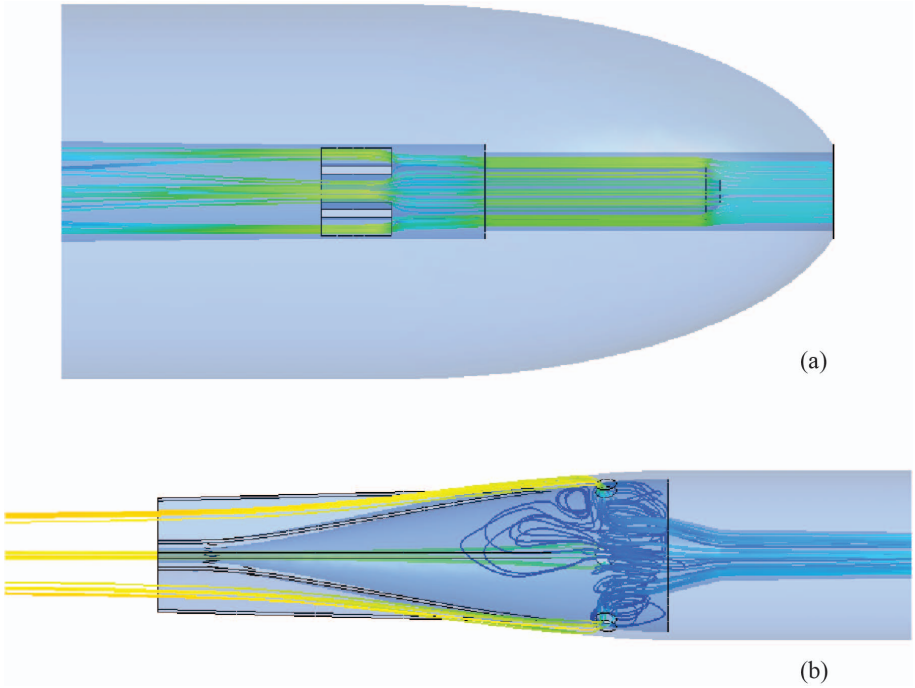

Fig. 3. Images of streamlines near the **(a)** probe inlet and **(b)** probe interior.

OSD
8, 1777–1802, 2011

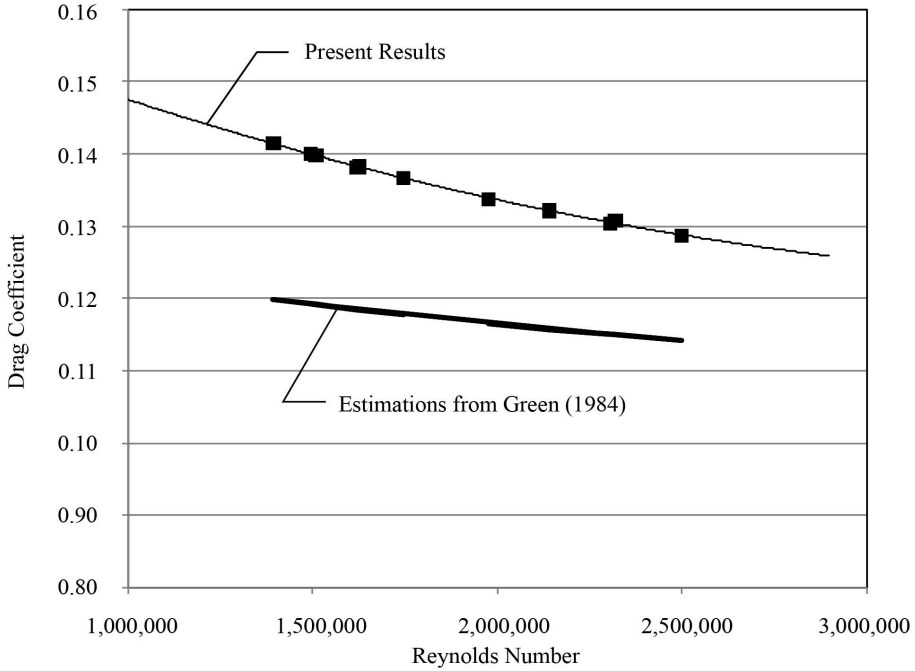

Fig. 4. Comparison of present drag coefficients with those from Green (1984).

OSD
8, 1777–1802, 2011

A computational method for determining XBT depths

J. Stark et al.

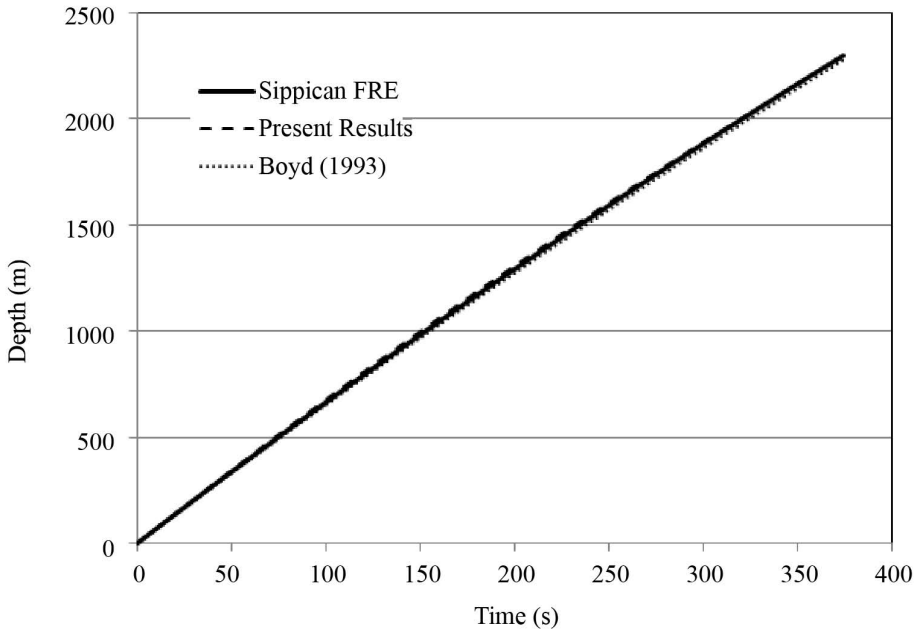

Fig. 5. Comparison of present depth results with manufacturer supplied FRE and the FRE from Boyd (1993).

OSD
8, 1777–1802, 2011

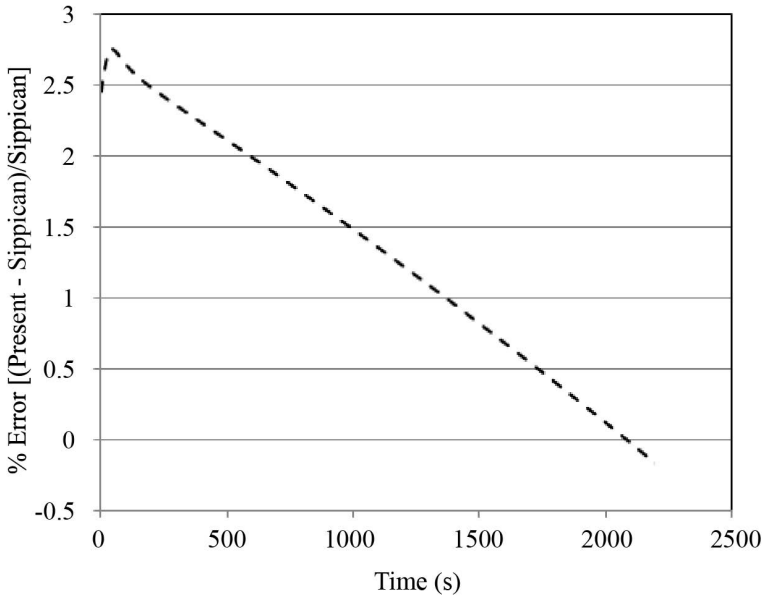

Fig. 6. Percent deviation of present results with predictions from the manufacturer supplied FRE.

OSD
8, 1777–1802, 2011

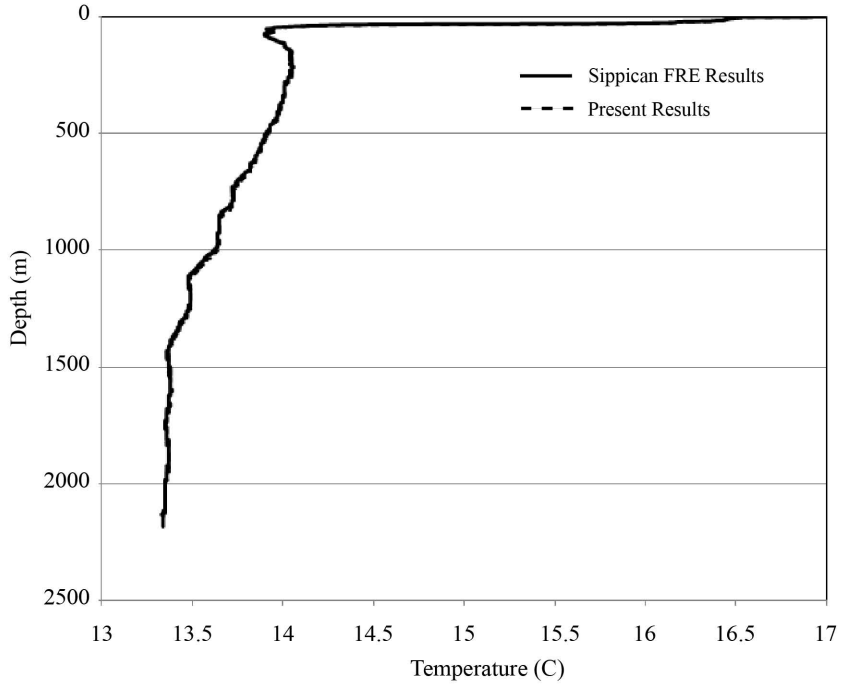

Fig. 7. Comparison of depth-temperature results, present results with manufacturer FRE.

OSD
8, 1777–1802, 2011